GEOPHYSICS, VOL. 59, NO. 9 (SEPTEMBER 1994); P. 1362-1376, 16 FIGS., 1 TABLE.

Detection of gas in sandstone reservoirs using AVO analysis: A 3-D seismic case history using the Geostack technique

Jan L. Fatti*, George C. Smith*, Peter J. Vail*, Peter J. Strauss*, and Philip R. Levitt*

ABSTRACT

The Geostack technique is a method of analyzing seismic amplitude variation with offset (AVO) information. One of the outputs of the analysis is a set of direct hydrocarbon indicator traces called "fluid factor" traces. The fluid factor trace is designed to be low amplitude for all reflectors in a clastic sedimentary sequence except for rocks that lie off the "mudrock line." The mudrock line is the line on a crossplot of P-wave velocity against S-wave velocity on which water-saturated sandstones, shales, and siltstones lie. Some of the rock types that lie off the mudrock line are gas-saturated sandstones, carbonates, and igneous rocks. In the absence of carbonates and igneous rocks, high amplitude reflections on fluid factor traces would be expected to represent gas-saturated sandstones. Of course, this relationship does not apply exactly in nature, and the extent to which the mudrock line model applies varies from area to area. However, it is a useful model in many basins of the world, including the one studied here.

Geostack processing has been done on a 3-D seismic data set over the Mossel Bay gas field on the southern continental shelf of South Africa. We found that anomalously high amplitude fluid factor reflections occurred at the top and base of the gas-reservoir sandstone. Maps were made of the amplitude of these fluid factor reflections, and it was found that the high amplitude values were restricted mainly to the gas field area as determined by drilling. The highest amplitudes were found to be located roughly in the areas of best reservoir quality (i.e., highest porosity) in areas where the reservoir is relatively thick.

INTRODUCTION

Ostrander (1982, 1984) showed that since gas-saturated sandstone layers have a lower Poisson's ratio than water-saturated sandstones, reflections at sandstone-shale interfaces have different amplitude variation with offset (AVO) response for the two cases. He also showed that this difference could be successfully used to detect gas-sandstones from surface P-wave seismic data.

Gassaway and Richgels (1983) and Russell (1988, 1990) showed that estimates of Poisson's ratio can be made by inverting AVO data from normal moveout- (NMO)-corrected common-midpoint (CMP) gathers using iterative matching techniques. Chiburis (1984, 1987) presented the AVO information of the target horizon as a ratio, relative to the amplitude of a shallower horizon. This approach removes the effect of factors other than the reflection coefficient on the variation of amplitude with offset and yields a very successful hydrocarbon indicator. Wiggins et al. (1984)* and Smith and Gidlow (1987) showed that P-wave and S-wave, zero-offset reflectivity traces can be computed by least-squares fitting of an approximation of the Zoeppritz equations to the reflection amplitudes within a CMP gather as a function of angle of incidence. Smith and Gidlow (1987) also showed that a computationally simpler procedure for doing the least-squares fitting can be achieved by a weighted stack of the traces in the CMP gather. They went on to show that the resulting P-wave and S-wave reflectivity traces can be combined to obtain "fluid factor" traces that can indicate the presence of gas. Gas sandstones in a clastic sequence give rise to high fluid factor amplitudes, while all other reflections have low amplitudes. The Smith and Gidlow procedure (Geostack), can be used to process large volumes

*There is a sign error in equation (6) of Wiggins et al. (1984). The sign of $\Delta V_p/V_p$ in the second term should be *minus*. This changes the resulting relationship between the shear reflectivity and the two coefficients derived from equation (6).

Presented at the 60th Annual International Meeting, Society of Exploration Geophysicists. Manuscript received by the Editor October 6, 1992; revised manuscript received October 26, 1993.
*Soekor, Piet van Zijl Building, 151 Frans Conradie Drive, Parow 7500, South Africa.

of data, and produces robust direct hydrocarbon indicator sections. The name Geostack signifies that it is a CMP stack based on a specific geophysical model of the reflected P-wave amplitudes.

In this paper, we present a case history of Geostack processing applied to a 3-D seismic survey over a gas field on the southern continental shelf of South Africa. The presence of gas is indicated on the Geostack-processed data by bright fluid factor reflections at the top and base of the gas reservoir sand stone. The spatial extent of the bright reflections corresponds roughly to the outline of the gas field as determined by drilling and structural mapping using the 3-D seismic data.

THE GEOSTACK TECHNIQUE

The starting point in Smith and Gidlow (1987) is an approximated form of the Zoeppritz equations after Aki and Richards (1980). Figure 1 shows the raypaths of the incident, reflected and refracted P-waves. V_1 is the P-wave velocity of medium 1, W_1 is the S-wave velocity of medium of 1, etc. The Aki and Richards equation gives an approximate relationship between the P-wave reflection coefficient and the angle of incidence:

$$R = \tfrac{1}{2}\,(AVIV + \Delta\rho/\rho) - 2(W/V)^2(2\Delta W/W + \Delta\rho/\rho)\sin^2\theta + \tfrac{1}{2}\,(\Delta V/V)\tan^2\theta, \qquad (1)$$

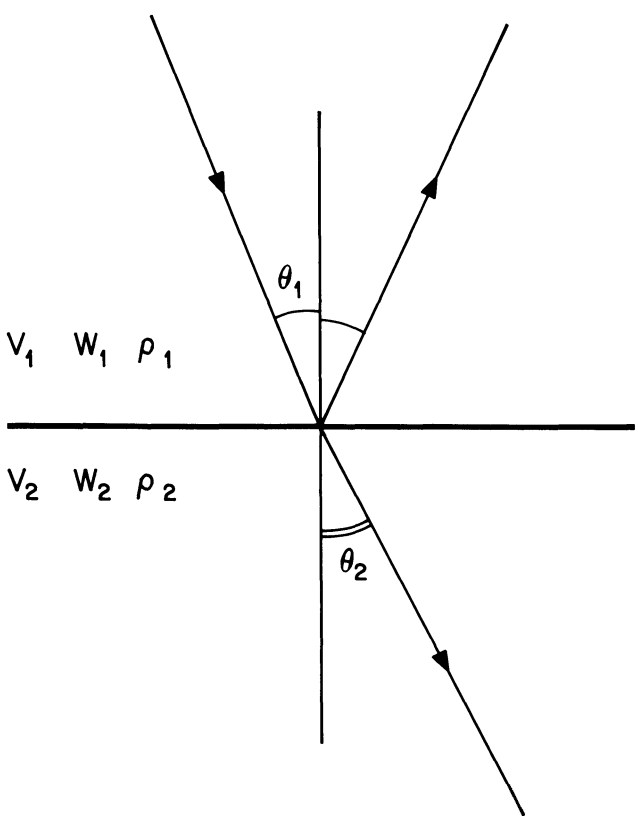

FIG. 1. Raypath diagram at the boundary between two layers showing the incident, reflected, and refracted P-waves. V is P-wave velocity, W is S-wave velocity, and ρ is density.

where

R = P-wave reflection coefficient
V = Average P-wave velocity (Average of V_1 and V_2)
W = Average S-wave velocity (Average of W_1 and W_2)
p = Average density (Average of ρ_1 and ρ_2)
θ = Average of θ_1 and θ_2
AV = $V_2 - V_1$, etc.

The assumptions made in equation (1) are:

1) $\Delta V/V$, A W/W and $\Delta\rho/\rho$ are sufficiently small that second order terms may be neglected.
2) θ does not approach critical angle or 90 degrees.

Equation (1) is accurate up to angles of incidence of around 50 degrees for typical velocity and density contrasts (Smith and Gidlow, 1987, Figures 2 and 3).

If Gardner's relationship between density and velocity holds true ($p = kV^{1/4}$, where k is a constant; Gardner et al., 1974), equation (1) becomes:

$$R = \Delta V/V(5/8 + \tfrac{1}{2}\tan^2\theta) - (W/V)^2(4\Delta W/W + \tfrac{1}{2}\,\mathrm{AVIV})\sin^2\theta. \qquad (2)$$

Alternatively, if Gardner's relationship does not hold, equation (1) can be rewritten in terms of P-wave and S-wave acoustic impedances: if $I = \rho V$, and $J = \rho W$, then $\frac{1}{2}\,\Delta I/I = \frac{1}{2}\,(\mathrm{AVIV} + \Delta\rho/\rho)$ = zero-offset P-wave reflection coefficient, and $\frac{1}{2}\,\Delta J/J = \frac{1}{2}\,(\Delta W/W + \Delta\rho/\rho)$ = zero-offset S-wave reflection coefficient. Now equation (1) can be rewritten as follows:

$$R = \tfrac{1}{2}\,\Delta I/I(1 + \tan^2\theta) - 4(W/V)^2(\Delta J/J)\sin^2\theta - [\tfrac{1}{2}\,(\Delta\rho/\rho)\tan^2\theta - 2(W/V)^2(\Delta\rho/\rho)\sin^2\theta]. \qquad (3)$$

It can be shown that the third term in equation (3) is small for angles of incidence (θ) less than 35 degrees and V/W ratio between 1.5 and 2.0 (Poisson's ratio between 0.1 and 0.33) (Gidlow et al., 1992, Figure 1). So equation (3) simplifies to:

$$R = \tfrac{1}{2}\,\Delta I/I(1 + \tan^2 0) - 4(W/V)^2(\Delta J/J)\sin^2\theta. \qquad (4)$$

Least-squares curve fitting is done to fit equation (2) or (4) to the P-wave reflection amplitudes from real data CMP gathers to estimate $\Delta V/V$ and A W/W [from equation (2)], or $\Delta I/I$ and $\Delta J/J$ [from equation (4)]. But before that can be done, a relationship must be determined between offset distance (x) and angle of incidence (θ), and we must also specify a value for *(W/V)*. We can estimate both the relationship and the *(W/V)* value if we know the P-wave velocity *(V)* as a function of depth or two-way time. A smooth P-wave velocity function against time for the area is obtained from a nearby well by severely smoothing the interval velocity function. The relationship between x and θ can then be determined by assuming the earth to be a stack of thin horizontal layers and performing iterative ray tracing. Ray tracing yields angle of incidence as a function of offset and zero-offset two-way time (Smith and Gidlow, 1987, Figure 4).

To determine *W/V*, we make use of the empirically derived "mudrock line" relationship between *V* and W for water-saturated elastic rocks determined by Castagna et al. (1985):

$$V = 1360 + 1.16W \text{ m/s}, \tag{5}$$

or a similar relationship determined from local measurements. Thus a W/V-against-traveltime function can be computed from the P-wave velocity function *(V).*

Curve fitting

It is shown in Smith and Gidlow (1987, Appendix A) that the least-squares curve fitting of equation (2) or (4) to the reflection amplitudes on common-midpoint (CMP) gathers can be expressed as a weighted sum of the reflection amplitudes in a CMP gather. In this way, we can solve for the unknowns $\Delta V/V$ and $\Delta W/W$ (or $\Delta I/I$ and *AJIJ)* at the boundary (i.e., the P-wave and S-wave zero-offset reflection coefficients). The reflection amplitudes are from conventional NMO-corrected CMP gathers. Thus $\Delta V/V$ and A W/W (or $\Delta I/I$ and $\Delta J/J$) reflection coefficient traces can be computed from weighted stacks of the traces in NMO-corrected CMP gathers. The two-way times of the resulting P-wave and S-wave zero-offset reflection coefficients for a specific reflector on the $\Delta V/V$ and A W/W traces are both the *same,* controlled by the *P-wave* velocity. This contrasts importantly with conventionally derived S-wave seismic sections where the S-wave event from a boundary arrives at a different time from the P-wave event because of the different *W* and *V* velocities. Of course, the $\Delta V/V$ and $\Delta W/W$ traces consist of wavelets rather than reflection coefficient spikes in the same way as conventional CMP-stacked traces do.

The two sets of weights to be applied to the samples of the CMP-gather traces (to produce the $\Delta V/V$ and A W/W traces, respectively) are computed from the *W/V* function, the angles of incidence and the number of traces (which varies with two-way time because of the far trace mute). The weights vary with offset and two-way time (Smith and Gidlow, 1987, Figures 5 and 6). The NMO-corrected traces in a CMP gather are multiplied by the weights and then summed. The resulting two traces are a zero-offset P-wave reflection trace and a zero-offset S-wave reflection trace where the two-way times of the events are the P-wave two-way times.

The fluid factor trace

The "fluid factor" concept was introduced in Smith and Gidlow (1987) to highlight gas-bearing sandstones. The crossplot of *V* against *W* in Figure 2 is derived from Castagna et al. (1985). Water-saturated sandstones, siltstones and shales fall approximately along the mudrock line. Gas-saturated sandstones have lower P-wave velocities and slightly higher S-wave velocities (Domenico, 1974) and therefore fall in the indicated gas zone. High-porosity sandstones fall at the low-velocity ends of the two sandstone clusters, and low-porosity sandstones fall at the high velocity ends. Castagna et al. (1985) give the equation of the mudrock line as:

$$V = 1360 + 1.16W \text{ m/s}.$$

Taking the derivative:

$$\text{AV} = 1.16\Delta W$$

$$\therefore (\Delta V/2V) = 1.16(W/V)(\Delta W/2W)$$

$$\text{i.e., } R_p = 1.16(W/V)R_s,$$

where R_p = zero-offset P-wave reflection coefficient

(velocity component only) = $\frac{1}{2}\,\Delta V/V$

and R_s = zero-offset S-wave reflection coefficient

(velocity component only) = $\frac{1}{2}$ A W/W

$$\therefore R_p - 1.16(W/V)R_s = 0$$

This relationship holds true *along the mudrock line.* We now define the "fluid factor," AF as:

$$\Delta F = R_p - 1.16(W/V)R_s. \tag{6}$$

If the layers above and below the boundary that produce a reflection lie on the mudrock line, then AF = 0. But if one of the layers lies on and the other lies off the mudrock line, then AF $\neq$ 0. For example, if one of the layers is a shale or a water sandstone and the other layer is a gas sandstone, this produces a nonzero value of AF. In a clastic sequence, we would expect nonzero values of AF at the top and base of gas-sandstones, but zero values of AF for all other boundaries. The amplitudes of the AF "reflections" from gas sandstones should be proportional to the separation between the gas sandstone and mudrock lines in Figure 2.

Another way of looking at equation (6) is: AF is the difference between the *actual* P-wave reflection coefficient R_p and the *calculated* R_p for the same sandstone in a water-saturated state. The calculated R_p is determined from the S-wave reflection coefficient *(R,)* using the local mudrock line relationship. From equation (6) we can write:

$$\Delta F(t) = R_p(t) - g(t)R_s(t), \tag{7}$$

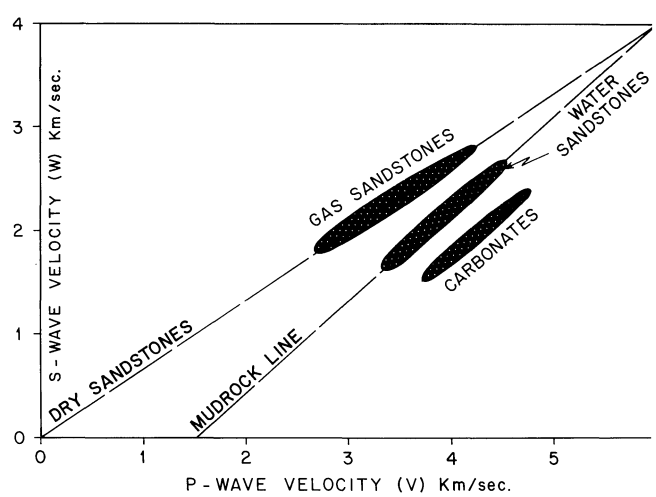

FIG. 2. Diagrammatic crossplot of P-wave velocity *(V* against S-wave velocity *(W)* (based on Castagna et al. 1985).

where

t = two-way time
AF(t) = fluid factor trace
$R_p(t)$ = P-wave reflectivity trace
$R_s(t)$ = S-wave reflectivity trace
$g(t)$ = $M(W/V)$ = a slowly time-varying gain function

and

M = Slope of the mudrock line, which can be an appropriate local value rather than that of Castagna et al. (1985).

The function g(t) is time-varying because W/V varies with time. One would also expect M, the slope of the mudrock line, to vary slightly from area to area, and probably with depth. It is thus useful to make crossplots of P-wave velocity against S-wave velocity from well measurements to determine the mudrock line for a particular area.

However, it is possible to estimate g(t) empirically from the R_p and R_s traces (Gidlow et al., 1992). A set of fluid factor [AF(t)] traces for about 20 adjacent CMPs are computed from equation (7), and this calculation is repeated for a series of constant g factors. The resultant panels of fluid factor traces are displayed side-by-side: the variation of g(t) is usually less than 4 dB over the typical zone of interest (1 .O to 2.8 s). A gain function g(t) which varies smoothly and slowly with time and which minimizes the energy in the AF(t) traces, is then picked by inspection. We call this analysis a gain function analysis. Such analyses are done at several locations over a prospect. It is assumed that the analysis is done at a location where there are no gas or oil sandstones, so the AF(t) traces should be low amplitude throughout. If there is a possible gas or oil sandstone or other lithology causing an anomaly on the gain function analysis panels, it should be recognized as such and excluded from the picking of the gain function.

Smith and Gidlow (1987) showed that for a space-invariant g(t) function, the fluid factor traces can also be computed directly from the CMP gather traces by using a particular set of weights.

Crossplots of P-wave velocity (V) against S-wave velocity (W)

Figure 3a is a crossplot of V against W from the gas reservoir interval of one of the Mossel Bay gas fields. These logs were derived from a recorded full-waveform sonic log. The following rock-type classification was used:

1) shale,
2) water-saturated sandstone, and
3) gas-saturated sandstone.

There is a good separation between water sandstone and gas sandstone, as predicted by Castagna et al. (1985). But there is also a separation between water sandstone and shale, which is contrary to their prediction that they lie on the same (mudrock) line. This means that weak AF reflections will occur at water sandstone/shale boundaries, as well as at water sandstone/gas sandstone boundaries. The strongest AF reflections will occur at shale/gas sandstone boundaries because of the large separation between the shale and gas-sandstone clusters.

If equation (4) is used instead of equation (2), crossplots of P-wave acoustic impedance (I) against S-wave acoustic impedance (J) are more appropriate. Figure 3b is a crossplot of I against J. The three rock types separate into linear trends as on the V against W crossplot (Figure 3a), and there is slightly less scatter of the points. The gas- and water-sandstone points in Figure 3b are displaced towards the lower left relative to Figure 3a because the sandstones have lower densities than the shales. The definition of AF [equation (7)] is now expressed in terms of $\Delta I/I$ and $\Delta J/J$ rather than A V/V and A W/W. As before, the amplitude of AF reflections depends on the separation between the gas-sandstone cluster and the shale and water-sandstone clusters in Figure 3b.

F-logs

In the same way that approximate acoustic impedance traces can be derived by integrating P-wave reflectivity traces, ‘ ‘F-impedance” traces can be derived by integrating equation (7) to give:

$$F = \ln V - \ln(X + MW), \tag{8}$$

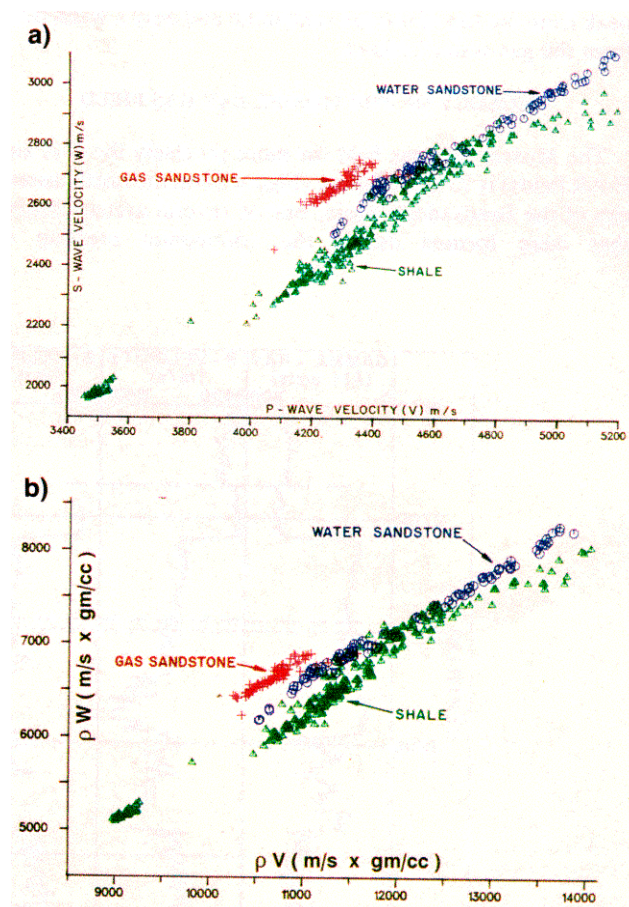

FIG. 3. (a) Crossplot of P-wave velocity (V) against S-wave velocity (W) for well F-AD1 in a satellite gas field close to the Mossel Bay Field and having a similar reservoir sequence to the Mossel Bay Field. (b) Crossplot of P-wave acoustic impedance (ρV) against S-wave acoustic impedance (ρW) for well F-AD1 .

where X and M are the intercept and the slope of the mudrock line, respectively. The expression (X + MW) is the value of *V* computed using the mudrock line for a rock with S-wave velocity *W*. If measured P-wave and S-wave velocity logs are available, the values of *V* and *W* can be substituted into equation (8) to obtain F-impedance logs, which we have named "F-logs." Of course, a local mudrock line may be used in equation (8). F should be close to zero for rocks near the mudrock line and negative for gas sandstones.

Figure 4 shows the F-log computed from the same *V* and *W* logs that were used in Figure 3. The gas sandstone stands out well as a negative F-log anomaly. It can be seen that the P-wave velocity in the gas-sandstone is lower than in the underlying water sandstone, but that the S-wave velocity in the gas sandstone is about the same as that in the water sandstone. This agrees with the results of Domenico (1974). Figure 5 shows a AF synthetic seismogram computed from the F-log in Figure 4. There is a strong trough from the top of the gas sandstone (horizon C), a strong peak from the base of the gas (GWC), and low amplitudes elsewhere. This agrees with the theoretically computed AF trace in Smith and Gidlow (1987, Figure 11). On the other hand, the zero-offset P-wave synthetic seismogram (Figure 5) has a peak from the top of the gas sandstone and only a weak peak from the gas-water contact.

GEOLOGY OF THE MOSSEL BAY GAS FIELD

The Mossel Bay gas field (or more precisely the F-A and F-AR fields) is 75 km offshore (Figure 6) on the northeastern rim of the Bredasdorp Basin, one of several arcuate basins that were formed during the continental breakup of

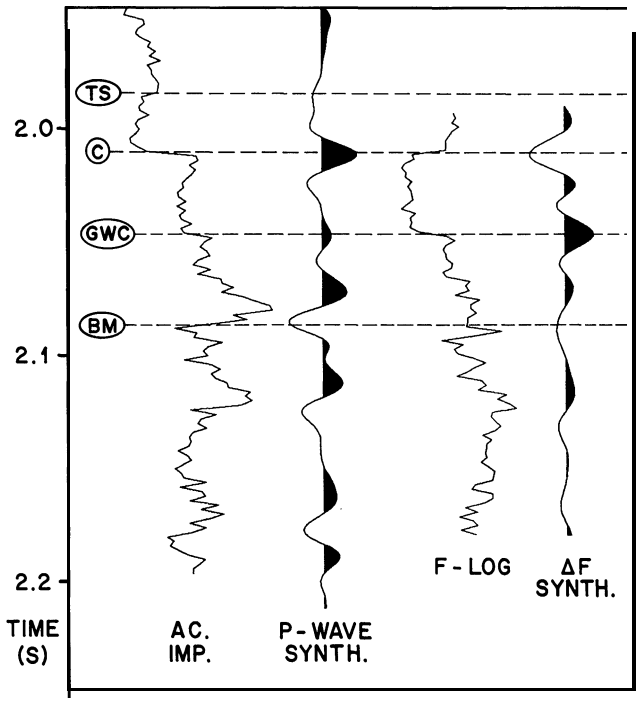

FIG. 5. Synthetic seismograms for well F-AD1 . From left to right: P-wave acoustic impedance; P-wave zero-offset synthetic seismogram (primaries only); F-log; fluid factor (AF) synthetic seismogram. The wavelet used was a zero-phase band-pass wavelet with corner frequencies of 2, 9, 40, and 57 Hz and positive standard polarity.

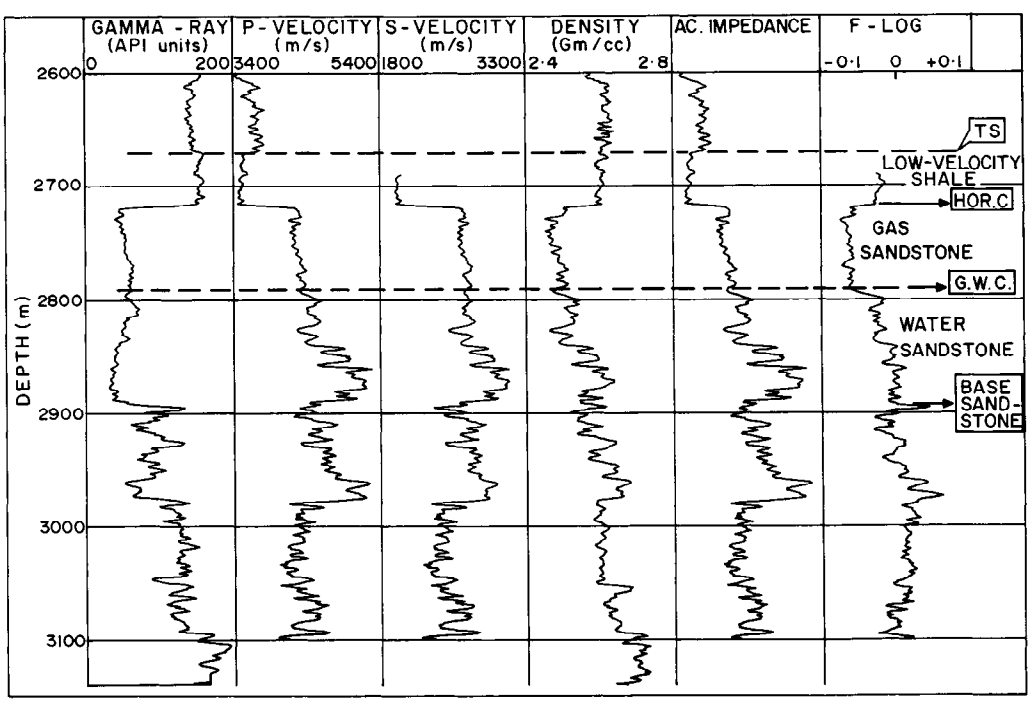

FIG. 4. Geophysical logs through the gas reservoir sandstone interval in well F-ADl.

Gondwanaland on the southern continental shelf of South Africa. Initial rifting began in the Jurassic, followed by successive periods of graben infill. The major marine incursion associated with final continental separation resulted in a major unconformity, horizon C, which forms the upper boundary of the gas reservoir sandstone (Fatti et al., 1994).

Figure 7 is a schematic north-south cross-section through the field. Figure 8 is the depth map of the top of the reservoir sandstone (horizon C) interpreted from the 3-D seismic data and the nine wells that are within the survey area. The field consists of two faulted structurally high areas, F-AR in the north and F-A in the south, separated by a syncline that overlies an older graben (Figure 7). The basement rocks consist predominantly of metamorphosed shales of Devonian age. They are overlain by four sedimentary depositional cycles. The first two cycles comprise a predominantly fluvial sequence. The following two cycles form the reservoir sandstone. They are of upper Jurassic age and were deposited in a nearshore shallow marine setting. These sandstone cycles grade upwards from fine-grained, poorly sorted sandstone to cleaner and better sorted medium-grained sandstone.

Overlying the reservoir interval and blanketing the horizon C unconformity is a succession of shales and siltstones of lower Cretaceous age and younger, deposited in open marine conditions during the drift phase of continental separation. There are north-south orientated major submarine canyons in the lower portion of this interval that erode into the reservoir sandstone and truncate it in places.

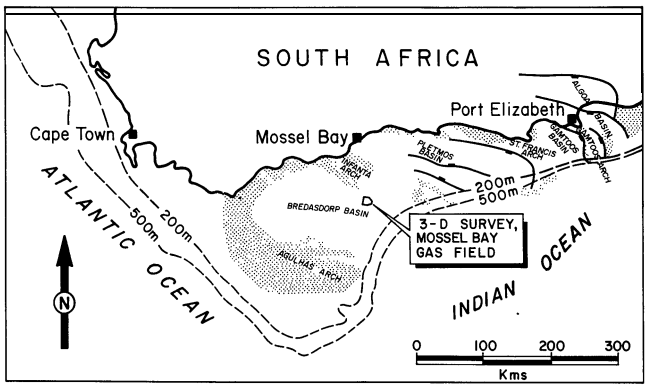

FIG. 6. Location map: southern coast of South Africa, showing the positions of the offshore basins and the Mossel Bay gas field. The shaded areas indicate shallow basement rocks.

THE 3-D SEISMIC SURVEY: ACQUISITION AND PROCESSING

The seismic lines were oriented along geological strike direction, west-northwest/east-southeast, because the predominant ocean swell is from the southwest. It has been found by experience that there is less recorded swell noise on lines that are shot parallel to the swell wavefronts rather than across them.

Acquisition parameters

The seismic lines were shot 50 m apart. The source was a 30-air-gun array of total volume 45 1. The streamer consisted of 240 hydrophone groups with a 12.5 m group interval, and the streamer depth was 10 to 12 m. The shotpoint interval was 25 m. There was usually a current from the northeast, deflecting the streamer southwards. The feathering angle varied between 0 and 18 degrees, averaging around 8 degrees.

Prestack processing

The Geostack processing was done differently from the conventional processing to ensure that the Geostack reflection amplitudes were not distorted. The prestack processing routes are given in Table 1.

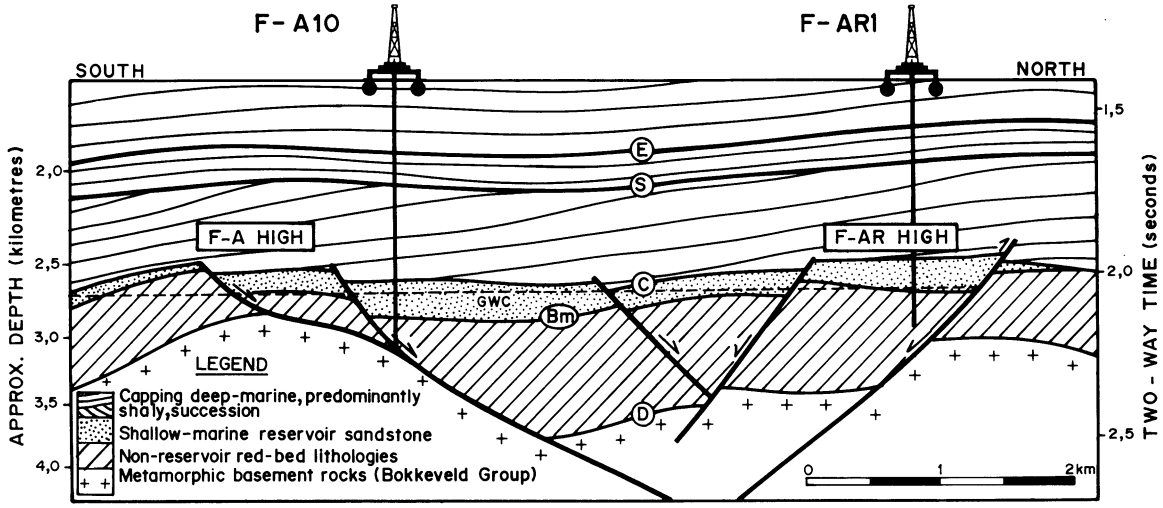

FIG. 7. Schematic north-south cross-section through the Mossel Bay gas field through wells F-AR1 and F-A10. The dashed line labeled GWC is the gas-water contact. The main seismic marker horizons are labeled E, S, C (horizon C unconformity), Bm (Base of shallow marine reservoir sandstone) and D (top of Devonian basement).

Table 1. Prestack processing routes for conventional and Geostack (AVO) processing.

Conventional processing	Geostack (AVO) processing
Spherical divergence correction	Spherical divergence correction ($V_{RMS}^2 t$)
	NMO correction (using a constant velocity function for the area)
F-K domain dipfilter (velocity filter)	F-K domain dipfilter
	Inverse NMO correction
	Array compensation filter, to correct for the effect of source and receiver arrays
Wavelet deconvolution with zero phase output (as described by Potts et al., 1982)	Wavelet deconvolution (Potts et al., 1982)
F-K domain multiple attenuation	
Traces sorted into rectangular bins	Traces sorted into rectangular bins
NMO correction	NMO correction
Trace equalization	Computation and application of R_p and R_s weights
Binned stack (50 fold)	Binned stack (56-fold) to produce R_p and R_s stacks

The reason for doing NMO correction before F-K dip filter in the AVO processing is to prevent distortion of the AVO of primary reflections by the dip filter (Dippenaar, 1989; Luh, 1992). The array compensation filter compensated for the source and receiver arrays up to the Nyquist wavenumber and was applied in the F-K domain. F-K multiple attenuation was not applied to the Geostack data, so as not to distort the amplitudes of primaries (F-K multiple attenuation usually attenuates the primaries at short offsets). "Elastic binning" was used for the Geostack processing to ensure that there was a full offset distribution of traces in each bin (i.e., if there was a missing offset in a bin, the bin was expanded until a midpoint with the appropriate offset was found). A milder prestack mute was used for Geostack than for the conventional data to include larger angle-of-incidence data.

Poststack processing

Since lateral and vertical velocity variation is fairly gradual, the 3-D migration could be done using a two-pass 2-D migration algorithm. The trace interval of the stacked traces was 25 m in the inline (strike) direction and 50 m in the crossline (dip) direction. The inline traces were migrated first. This was followed by trace interpolation in the crossline direction to reduce the trace interval from 50 m to 12.5 m before crossline migration.

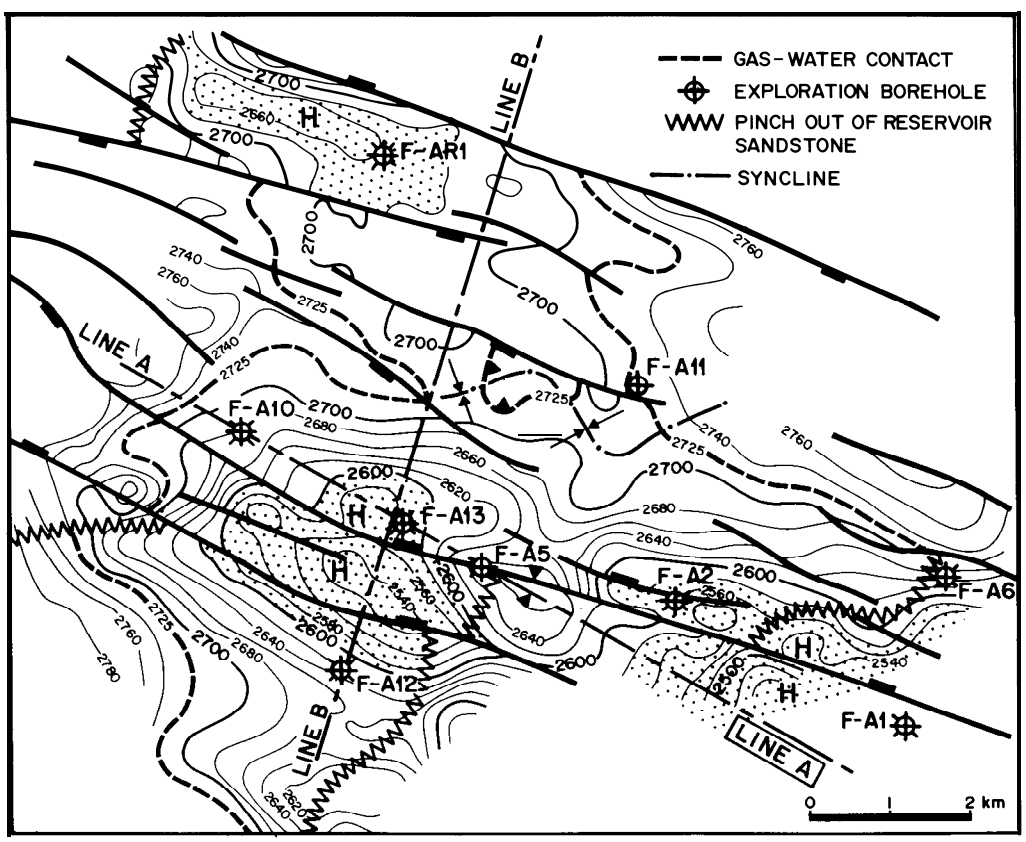

FIG. 8. Depth structure contour map of the top of the shallow marine gas reservoir sandstone (horizon C unconformity) as interpreted from the 3-D seismic data. Contour interval is *20* m. The locations of seismic lines A and B (Figures 10 and 11) are indicated. The shaded areas are structural highs.

Conventional poststack processing sequence.-

1) Deconvolution (predictive deconvolution, with gap length equal to 90 percent of the two-way time through the water layer, which is about 140 ms)
2) Inline migration (Finite-difference algorithm)
3) Crossline interpolation (from 50 m to 12.5 m trace interval)
4) Crossline migration
5) Deterministic inverse Q-filter
6) Time-variant, band-pass filter
7) Mild AGC
8) Residual phase correction to zero phase.

The residual phase correction filter was computed from cross-correlations at the well locations between the zero-phase P-wave normal incidence synthetic seismograms and the corresponding 3-D migrated traces. The same phase correction filter was used for the whole survey since the residual phase estimate was very similar at all the wells.

Geostack (AVO) poststack processing sequence.-Accurate NMO correction is very important in AVO analysis. Very detailed velocity analysis was therefore done to determine the stacking velocity field accurately. A smooth time-varying gain function (constant for the whole survey) was applied to the R_p and R_s traces to balance the amplitudes from top to bottom. The R_p and R_s traces were then combined according to equation (7) to produce the AF traces. Gain function analyses were done at several locations over the survey. The gain functions [g(t)] picked from these analyses were very similar, so they were averaged. The average gain function, which varied slowly and smoothly with time, was used for the whole survey. Over the zone of interest (1.4 to 2.6 s), the gain function varied by less than 1 dB.

The only processing of the AF traces was: inline migration, crossline interpolation, crossline migration, and residual phase correction. Poststack deconvolution and inverse Q-filtering were not included in the Geostack processing in case these processes produced amplitude distortion.

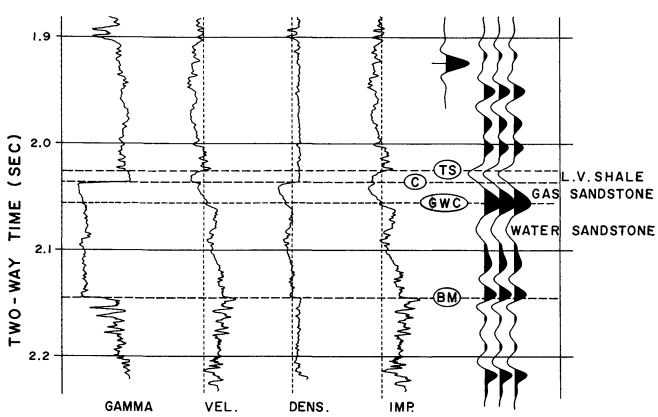

FIG. 9. Zero-offset P-wave synthetic seismogram of the reservoir interval at well F-A10. From left to right: gamma-ray log, P-wave velocity, density, P-wave acoustic impedance, wavelet used for the synthetic (corner frequencies 2,9, 40, and 57 Hz), and the synthetic traces (primaries only, positive standard polarity). Marker horizons are labeled TS (top of low velocity shale), C, GWC (gas-water contact), and BM (base of shallow marine sandstone).

Comparison between the R_p sections (zero-offset P-wave sections) and the conventionally stacked sections showed higher multiple reflection energy in the R_p sections. This is because of the omission of *F-K* multiple attenuation and poststack deconvolution from the Geostack processing, and also because the R_p weights downweight the outside traces in the CMP gathers (Smith and Gidlow, 1987, Figure 5). The amplitude of multiples on the fluid factor (AF) sections was lower than on the R_p sections because the notional AF weights downweight the inner traces relative to the outer traces in the CMP gathers below 1.5 s (Smith and Gidlow, 1987, Figure 8). This causes the multiples to be better attenuated on the AF traces than on the R_p traces.

THE GEOSTACK RESULTS

Figure 9 is a P-wave zero-offset synthetic seismogram of the reservoir interval in well F-A10. A zero-phase, band-pass wavelet was used with corner frequencies 2, 9, 40, 57 Hz, primary reflections only. An l&m-thick, low-velocity shale unit (about 10 ms two-way time) directly overlies the gas-reservoir sandstone as can be seen on the velocity log. This shale and the gas reservoir both have low acoustic impedances, with little impedance contrast between the two, and consequently there is almost no reflection from the top of the gas reservoir (horizon C) at normal incidence. There are fairly strong reflections from horizon TS, the top of the low velocity shale, (negative reflection coefficient, producing a reflection trough), and from the gas-water contact (positive reflection coefficient, producing a reflection peak). In some of the other wells, owing to the gas-reservoir sandstone having lower porosity and thus higher acoustic impedance, there is an impedance increase at the top of gas reservoir, which produces a positive reflection coefficient (i.e., a peak). Well F-AD1 in a nearby satellite gas field illustrates this effect (Figures 4 and 5). The response of the top of gas reservoir (horizon C) varies across the field between a weak negative reflection coefficient in some areas to a positive reflection coefficient in other areas. But the horizon C reflection is obscured by the stronger overlying horizon TS in most areas.

Figure 10a and Figure lla are the conventionally processed 3-D migrated sections of lines A and B displayed in variable density. Their locations are indicated in Figure 8, the depth structure-contour map of the top of the reservoir sandstone, interpreted from the 3-D survey. Figure l0b and Figure llb are the corresponding migrated fluid factor sections with horizon annotations, and Figure 10c and Figure 1 lc are the fluid factor sections without annotations. Positive reflection coefficients correspond to black (peaks) in these displays. Horizon TS, the top of the low velocity shale, is a prominent trough (white) event on the conventional sections at about 2.0 s. In Figure 10a it disappears west of well F-A10 where the low-velocity shale and the gas-bearing upper portion of the shallow marine sandstone reservoir have been removed by later channel erosion. The erosion is produced by two north-south trending deep marine clay-filled channels. The base of the channel erosion is indicated as CE in Figure l0b. East of well F-A5 the low velocity shale and the shallow marine sandstone have been completely removed by channel erosion (on the upthrow side of the fault). At well

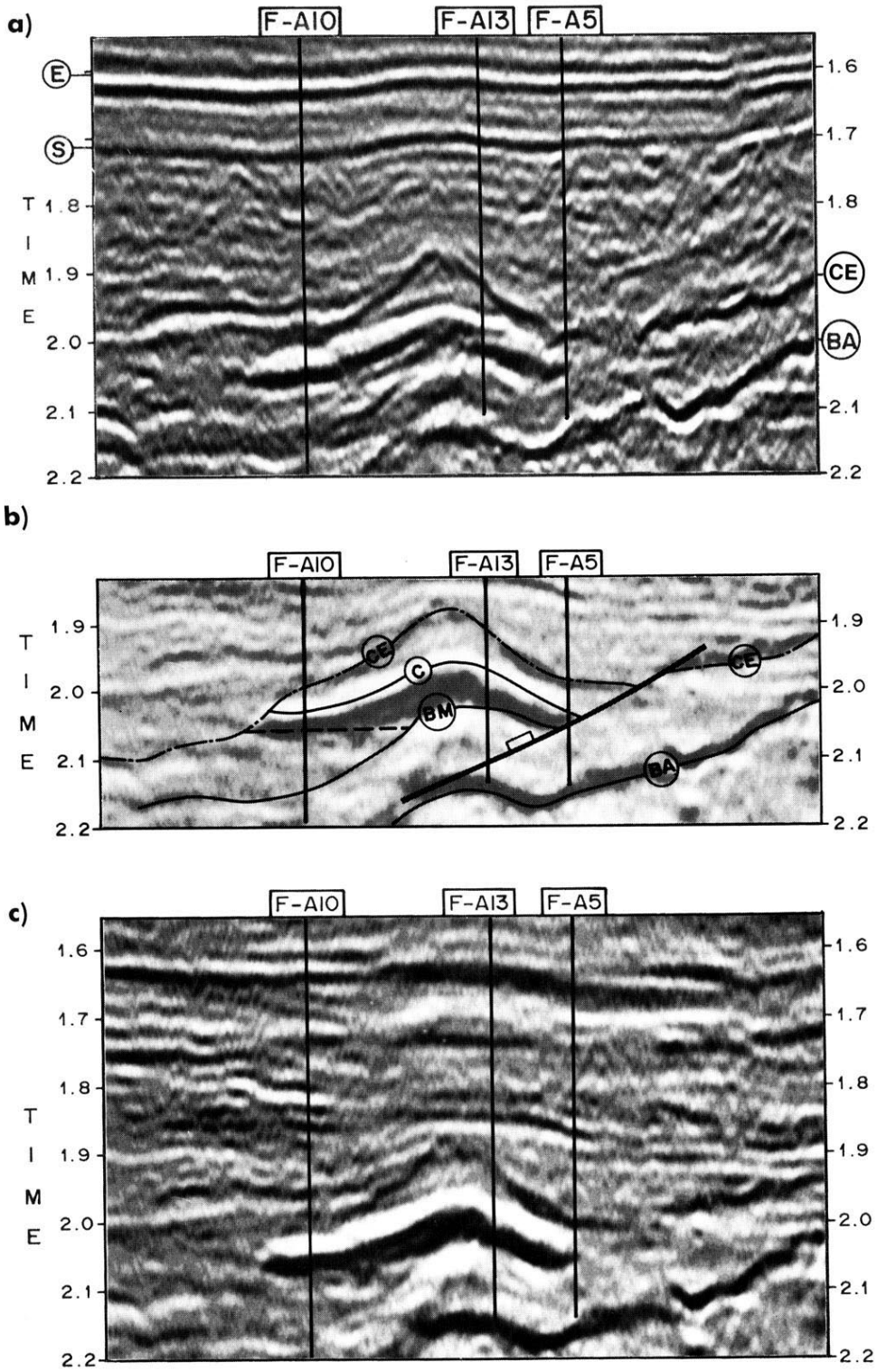

FIG. 10. (a) Conventionally processed seismic action of line A, positive standard polarity and variable density mode. See Figure 8 for location. Positions of wells are indicated. Horizon TS is the trough (white) at 2.03 s at F-A10, and 2.0 s at F-A13. (b) Fluid factor section of line A with seismic horizons indicated: CE = base of channel erosion; C = horizon C; horizontal broken line at 2.05 s is the gas-water contact; BM = base of shallow marine reservoir sandstone; BA = top of basement. (c) Fluid factor section of line A.

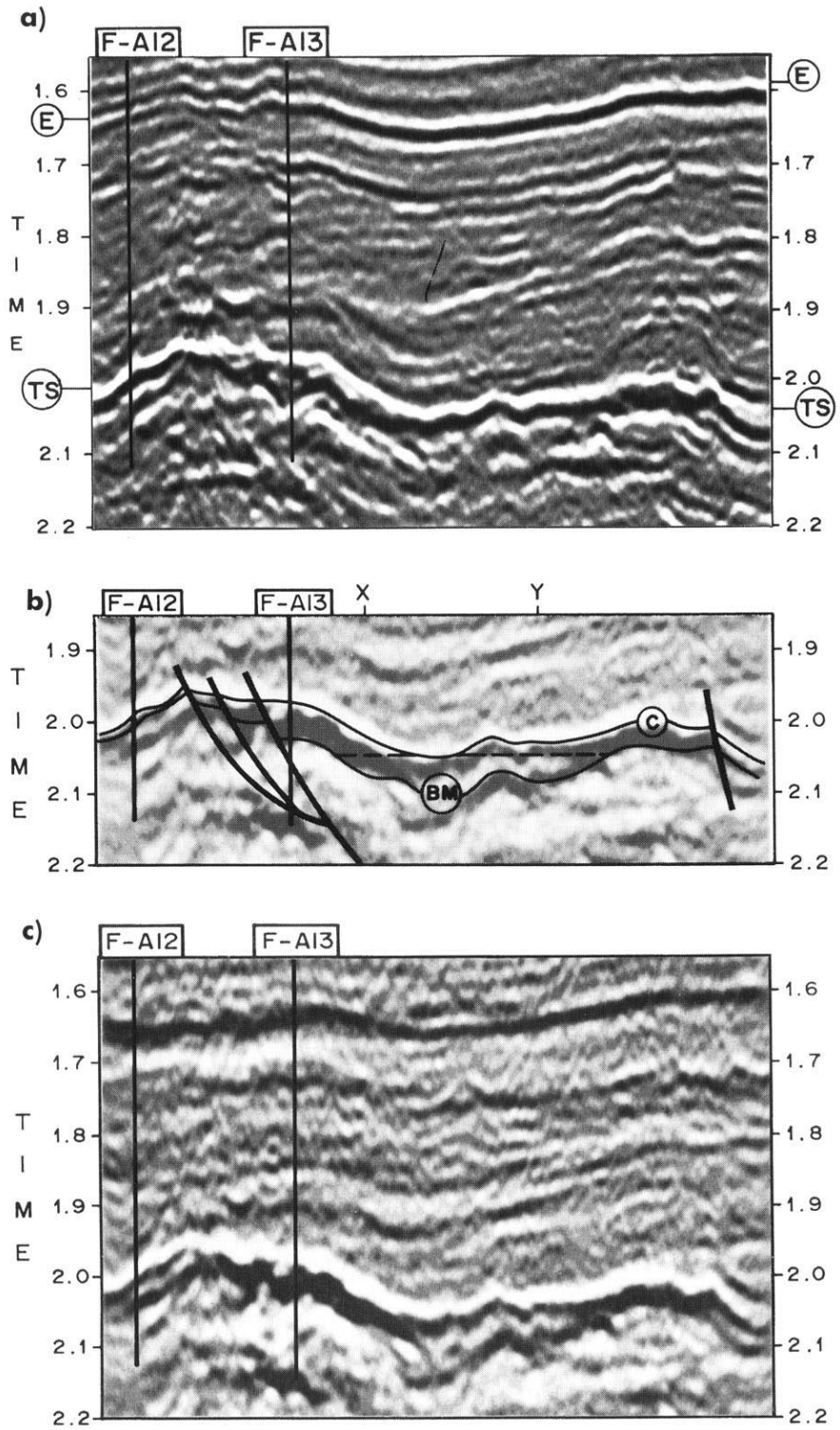

FIG. 11. (a) Conventionally processed seismic section of line B, which is approximately in the dip direction (south-southwest-north-northeast). See Figure 8 for location. The main F-A structural high is on the left (south), and the F-AR high is on the right (north). (b) Fluid factor section of line B with seismic horizons indicated: C = horizon C (top of gas reservoir sandstone); horizontal broken line at 2.05 s is the gas-water contact; BM = base of shallow marine reservoir sandstone. (c) Fluid factor section of line B.

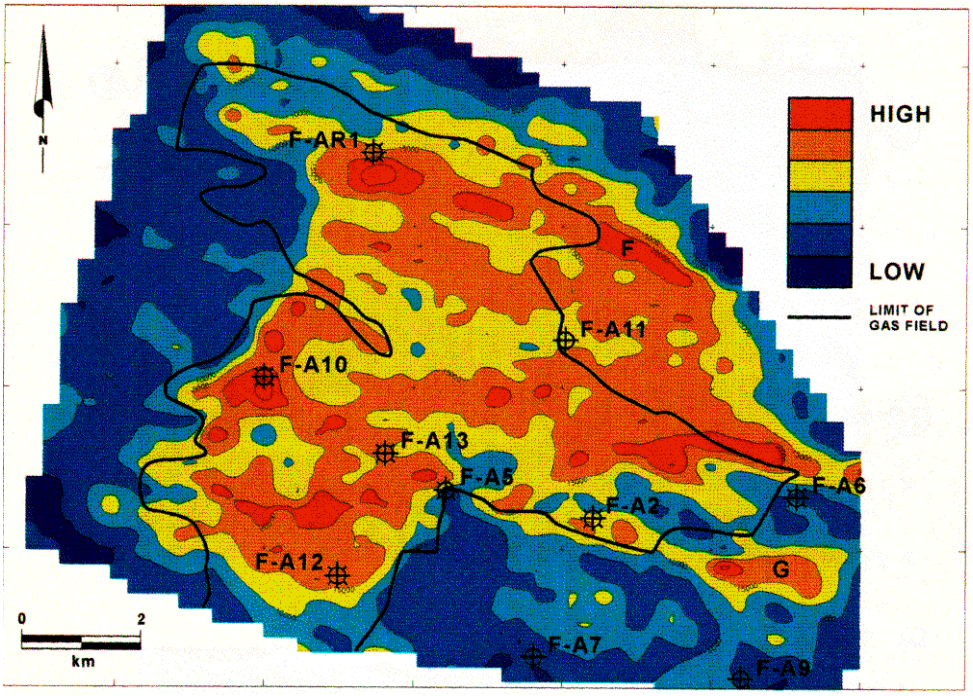

FIG. 12. Fluid factor amplitude map of the top-of-gas-reservoir event (horizon C). This event is a trough (negative number). The absolute value has been mapped.

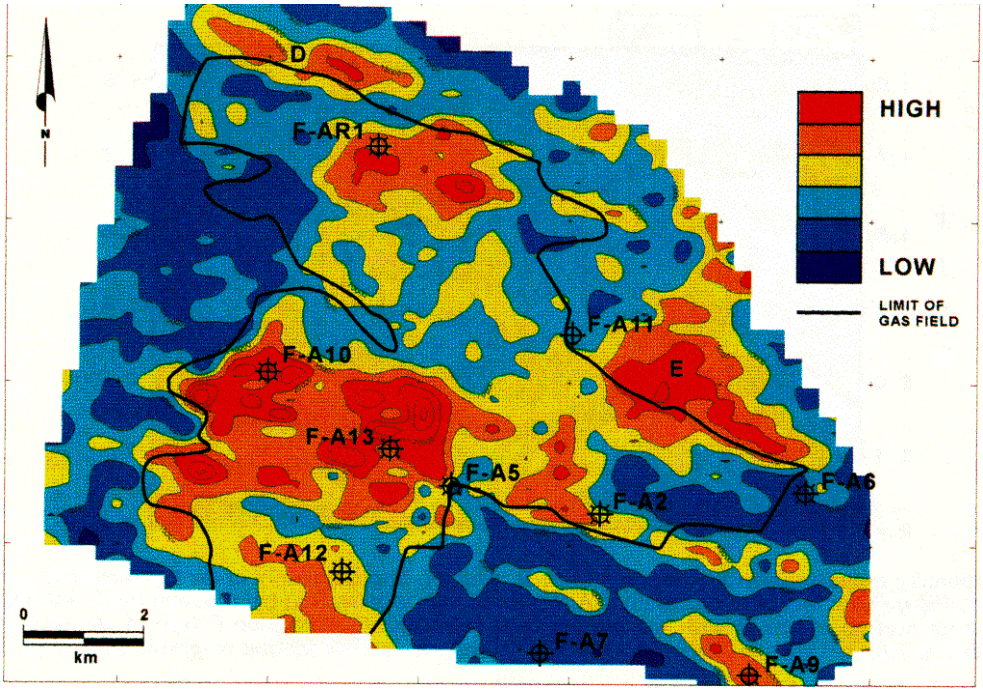

FIG. 13. Fluid factor amplitude map of the base-of-gas event (horizon BG). This event is a peak.

F-A10 in Figure 10a there is a strong positive reflection at the gas-water contact (2.050 s) caused by the large impedance increase shown in Figure 9. A weak gas-water contact is also seen in places on the conventional data north of well F-Al3 but is not very prominent overall. This reflection can be seen in some areas at approximately position X of Figure 1 lb.

On the fluid factor sections (Figures 10c and llc) the gas-sandstone response is a strong trough from the top (horizon C), followed by a strong peak. The peak (horizon BG) is from the gas-water contact at well F-A10 (Figure l0b), but in most areas it is from the base of the porous upper zone of the gas-sandstone. This zone is up to 50 m thick, with porosities between 15 and 22 percent.

As one would expect from the theory, the fluid factor sections (Figure 10c and Figure 1 lc) have an overall fairly low amplitude except at the gas reservoir level, which is high amplitude. Most of the events above the gas-sandstone, including the strong events at horizons E and S (about 1.6 and 1.7 s) in Figure l0a, are weaker on the fluid factor section than on the conventional section. The fluid factor sections are slightly lower frequency overall than the conventional sections because of the effect of NMO-stretch and the heavier weighting of the outside traces relative to the inside traces by the notional AF weights (Smith and Gidlow, 1987, Figure 8), and also because the fluid factor sections have no inverse-Q filter.

Because there is a slight separation between shale and water-sandstone points on the *V* against W crossplot, one would expect weak fluid factor reflections from water sandstones within a shale sequence. This probably explains some of the weak events above horizon C in Figure 10c and Figure 1 lc. The strong deep event dipping to the left in Figure 10c (2.15 s at well F-A5) is the top of basement (Devonian shales). The reason why this fluid factor reflection is high amplitude is probably because there is a large P-wave acoustic impedance contrast here, which violates one of the assumptions in equations (l)-(4).

Figure 12 and Figure 13 are fluid factor amplitude maps of the top-of-gas and base-of-gas events, respectively. They were derived from the amplitudes of the horizon C and BG events, picked using an interactive 3-D interpretation workstation. Only full-fold, properly migrated traces were used to make these maps, so there are no edge effects. On both maps there are high-amplitude anomalies that lie roughly within the known limits of the field. (The field limits are determined by the gas-water contact on most sides, and by erosional pinch outs or faults on the other sides).

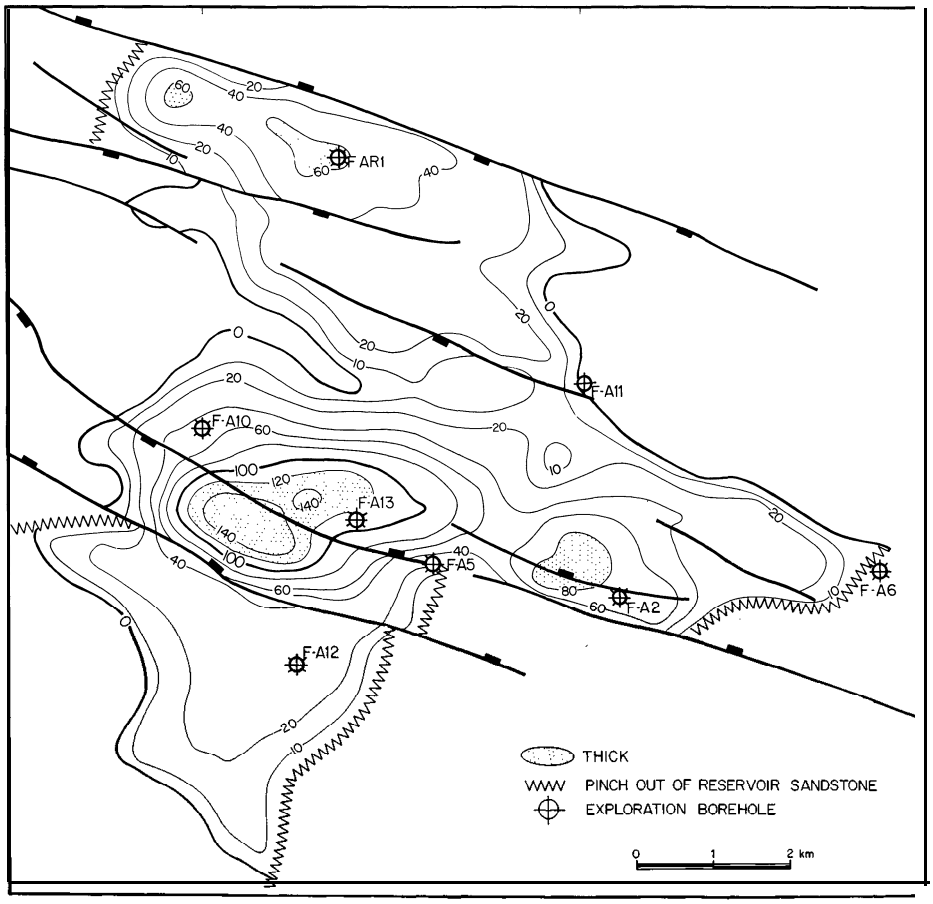

FIG. 14. Isopach (thickness) contour map of the gas reservoir interval as interpreted from the 3-D seismic data and the wells. Contour interval is 20 m.

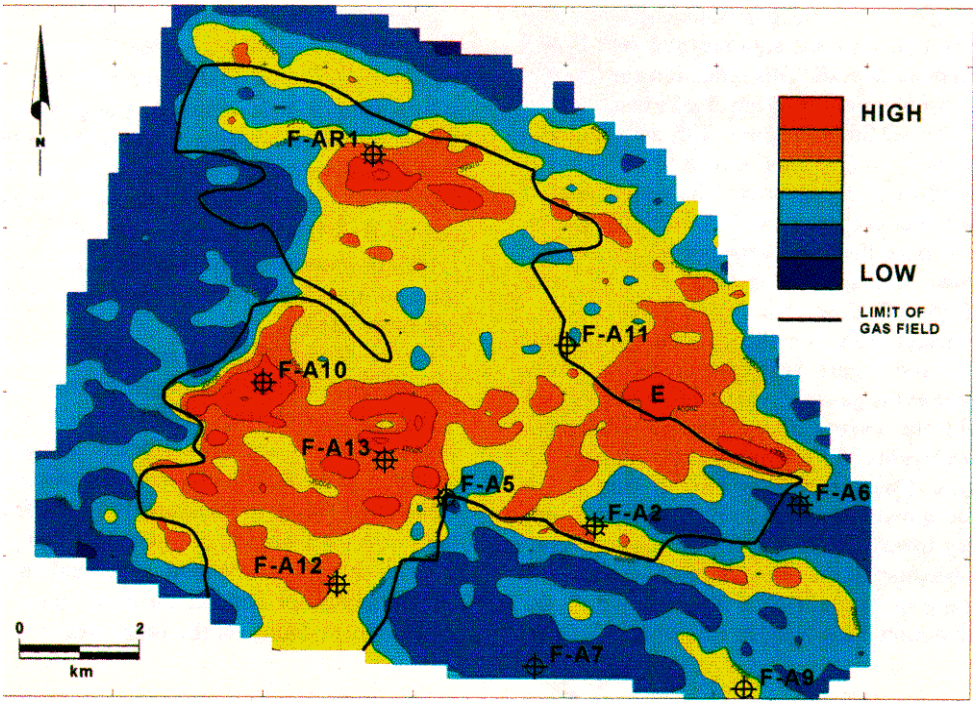

FIG. 15. Sum of the two fluid factor amplitude maps: top-of-gas reservoir, and base of gas (Figures 12 and 13).

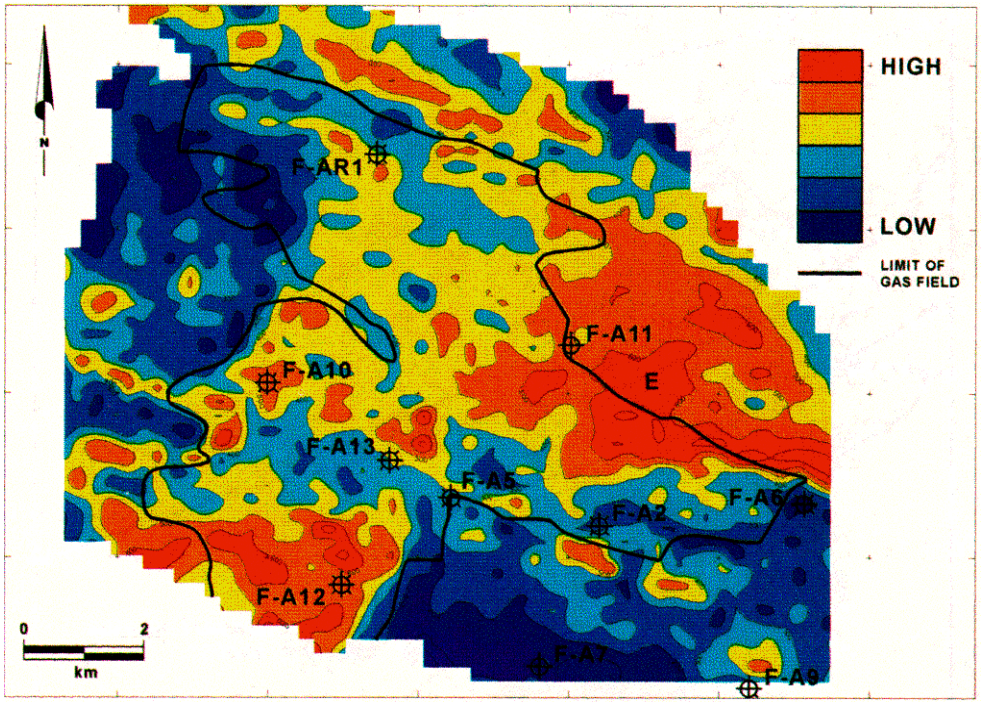

FIG. 16. Map of maximum value of the amplitude envelope of the conventional seismic data at the top-of-gas-reservoir level (horizon TS/horizon C).

Except for the anomaly labeled E in Figure 13, the high amplitude anomalies on the base-of-gas map are located roughly in the thick parts of the reservoir and where the reservoir quality is good (i.e., where the porosity is high and *V* is low, and therefore there is a large separation between the mudrock and gas-sandstone lines on the *V* against W crossplot). The isopach map of the gas-bearing interval (Figure 14) shows that the thickest parts of the reservoir are west of well F-Al3 on the southern structural high and at well F-AR1 on the northern structural high.

Figure 15 is the sum of the absolute values of the two amplitude maps (top and base). In this figure, the highest amplitude areas again correspond roughly to thick parts of the gas reservoir or where reservoir quality is good. However, on the northeast side of the field, the high amplitude area extends beyond the mapped limit of the gas field, below the gas-water contact. The high amplitude anomaly labeled E in Figure 13 and Figure 15, east of well F-A11, could possibly be an untested extension of the field with a stratigraphic permeability barrier or fault as the trapping mechanism. There was no gas in well F-Al 1. The reservoir in this well was just below the gas-water contact depth, and was water-saturated.

On the base-of-gas amplitude map (Figure 13) there is a narrow high-amplitude anomaly northwest of well F-ARl, north of the northern limit of the field (labeled D). This anomaly could be produced by a possible small extension of the field north of the northern fault boundary of the field (Figure 8). High amplitude anomaly G in Figure 12 (southeast of well F-A2) falls within a narrow fault block that is structurally deformed, and hence the amplitudes here are considered to be unreliable. However, it is possible that a sliver of gas-bearing sandstone is present at this location.

Figure 16 is a map of the maximum value of the amplitude envelope of the conventionally processed data at the level of top of reservoir (horizon TS/horizon C). The amplitude envelope was used here instead of the amplitude of the top of reservoir itself because the top-of-reservoir reflection (horizon C) is weak on the conventional data (Figure 9) and changes over different parts of the field from a trough to a zero-crossing to a peak. This map should be compared to the trough-plus-peak fluid factor amplitude map (Figure 15), which might be expected to be similar to an amplitude envelope map.

There are high amplitudes over parts of the gas field in Figure 16, but the location of the gas field is indicated better by the high amplitudes on the fluid factor map (Figure 15) than on the conventional data map. Also, the thickest portions of the gas sand (west of F-A13, west of F-A2, and at F-AR1) in Figure 15 have higher amplitudes than in Figure 16. It must be remembered that the amplitudes in Figure 16 are also affected by horizon TS, the high amplitude reflection directly above horizon C, which is unrelated to the gas sandstone (Figure 9).

The edge of the high amplitude west of F-A10, on both the Geostack and conventional amplitude maps is very sharp because both the gas-bearing upper part of the shallow marine sandstone reservoir and the overlying low velocity shale have been removed here by channel erosion (Figure l0b).

The area northeast of the field, which is high amplitude on the fluid factor maps, is also high amplitude on the conventional data. This behavior cannot be explained at present. It could be an extension of the gas field, as mentioned earlier, but it might possibly also be an area of unusual lithology, not intersected in any of the wells.

CONCLUSIONS AND DISCUSSION

There are high-amplitude fluid factor reflections from the top and base of the gas reservoir sandstone. The highest fluid factor amplitudes occur in areas of thick gas sandstone, roughly in the areas of best reservoir quality (highest porosity). The high amplitude anomalies are restricted mainly to the known gas field area and terminate roughly at the edge of the field. On the conventionally processed data, there is also a high amplitude event at the top of the gas sandstone, but this event is produced mainly by the reflection from the top of the low velocity shale overlying the gas-sandstone reservoir (horizon TS). The reflection from the top of the gas sandstone itself is weak. The high amplitude area on the fluid factor maps is a better indicator of the outline of the gas field than the amplitude map of the conventional data. We conclude that the Geostack technique is a direct hydrocarbon indicator of gas in this area.

In the central Bredasdorp Basin, about 70 km southwest of the Mossel Bay gas field, some success has also been achieved in detecting oil-saturated sandstones using Geostack. These sandstones are in lower Cretaceous deep marine turbidite fans at similar depths to the Mossel Bay gas field. Hwang and Lellis (1988) have reported that the P-wave velocity of oil can be very low because of dissolved gas. This causes oil sandstone to be located close to gas sandstone on the *V* against *W* crossplot (Figure 2), and thus produces a AF reflection.

The success of the AF (fluid factor) traces in indicating the presence of gas depends on the amount of separation on the *V* against *W* crossplot (Figure 2) between gas sandstones on the one hand and water sandstones and shales (the mudrock line) on the other hand. There is a clear separation between gas sandstone and water sandstones in the F-A gas field (Figures 3a and 3b), but unfortunately shale and water sandstone do not fall on exactly the same line as each other. Thus one would expect weak fluid factor reflections from boundaries between shale and water sandstones, as well as stronger reflections from shale/gas-sandstone boundaries. This behavior is confirmed by the fluid factor sections over the F-A gas field (Figure 10c and Figure 1 lc).

All the other well known effects that control the amplitude of P-wave reflections and therefore AVO measurements also affect the success of the Geostack method. Included in these effects are residual NMO correction errors, absorption and transmission effects in overlying beds, anisotropy in overlying shales, and thin-bed tuning. The effect of some of these factors can be reduced empirically to a certain extent by choosing the gain function g(t) so as to minimize the AF trace amplitudes in non-gas-bearing sequences [equation (7)]. In the F-A survey, g(t) changed slightly with time but not spatially. Changing the factor g corresponds to moving the position of the mudrock line in Figure 2.

A problem that still needs to be addressed in this data set is the attenuation of interbed multiples on the fluid factor sections, using a technique that will not change the AVO

behavior of primary reflections (Foster and Mosher, 1992). The weak event dipping to the right in Figure 10c at about 1.9 s is probably a residual multiple.

The following final comments can be made about the Geostack method:

1) The ideal environment for Geostack is a elastic sequence without carbonates or igneous rocks. Carbonates fall on the opposite side of the mudrock line to gas-sandstones (Figure 2), and lavas also fall in the same region (Klimentos, 1991). Carbonate and igneous rock layers therefore also produce fluid factor anomalies, but of opposite polarity to gas sandstones. Thus, if the fluid factor traces have been corrected to zero phase, one should be able to distinguish between the two classes of anomalies based on their polarities.

2) Fluid factor traces are better gas indicators than are "amplitude gradient" traces, where amplitude gradient is the gradient of a straight-line fit of the P-wave reflection amplitudes on a plot of amplitude against $\sin^2\theta$ (Walden, 1991). Amplitude gradient traces highlight reflection amplitudes that increase with offset, which happens when the gas sandstone has lower acoustic impedance than the encasing shale (class 3 sandstones of Rutherford and Williams, 1989). It is more difficult to locate gas sandstones with higher acoustic impedance than the encasing shale using the amplitude gradient method (class 1 sandstones). Fluid factor traces, on the other hand, should contain high amplitude events whether the gas sandstone impedance is lower, the same as, or higher than the shale (class 3, 2, or 1 sandstones). This behavior results because the only requirement for a AF anomaly is that the gas sandstone and the mudrock (or shale) lines should be separate on the *V* against W crossplot. Also, equations (2) or (4) used in Geostack are accurate to larger angles of incidence than the 25-degree approximation that is sometimes used in the amplitude gradient method [Walden, 1991, equation (l)].

ACKNOWLEDGMENTS

The acquisition of the 3-D seismic survey was done by the survey ship EXPLORA, of Prakla-Seismos, Hannover, Germany. The processing of the data was done by GSI in Bedford, UK, and was supervised by Glyn Roberts and Neil Ratnett. We thank Prof. Milo Backus for constructive and useful suggestions that resulted in improvements to the paper. We thank Maurice Gidlow for helpful suggestions, and Lance Holmes and Andy Jollands for helpful discussion on the geology of the F-A field. We also thank the Soekor drawing office staff for draughting the illustrations, and the Soekor management for permission to publish the paper.

REFERENCES

Aki, K., and Richards P. G., 1980, Quantitative seismology: W. H. Freeman and Co.

Castagna, J. P., Bazle, M. L., and Eastwood, R. L., 1985, Relationships between compressional-wave and shear-wave velocities in elastic silicate rocks: Geophysics, 50, 57 l-58 1.

Chiburis, E. F., 1984, Analysis of amplituded versus offset to detected gas/oil contacts in the Arabian Gulf: 54th Ann. Intemat. Mtg., Soc. Expl. Geophys., Expanded Abstracts, 669-670.

- 1987, Studies of amplitude versus offset in Saudi Arabia: 57th Ann. Intemat. Mtg., Soc. Expl. Geophys., Expanded Abstracts, 614-616.

Dippenaar, A. T., 1989, A new approach to velocity filtering: First Tech. Mtg., S. Afr. Geophys. Assoc., Expanded Abstracts, 37-40.

Domenico, S. N., 1974, Effect of water saturation on seismic reflectivity of sand reservoirs encased in shale: Geophysics, 39, 759-769.

Fatti, J. L., Strauss, P. J., and Stallbom, K., 1994, A 3-D seismic survey over the offshore F-A gas field: S. Afr. Geophys. Rev., 1, l-22.

Foster, D. J., and Mosher, C. C., 1992, Suppression of multiple reflections using the radon transform: Geophysics, 57, 386-395.

Gardner, G. H. F., Gardner, L. W., and Gregory, A. R., 1974, Formation velocity and density, the diagnostic basics for stratigraphic traps: Geophysics, 39, 770-780.

Gassaway, G. S., and Richgels, H. J., 1983, SAMPLE: Seismic Amplitude measurement for primary lithology estimation: 53rd Ann. Intemat. Mtg., Soc. Expl. Geophys., Expanded Abstracts, 610-613.

Gidlow, P. M., Smith, G. C., and Vail, P. J., 1992, Hydrocarbon detection using fluid factor traces, a case study: How useful is AVO analysis? Joint SEG/EAEG summer research workshop, Technical Program and Abstracts, 78-89.

Hwang, L. F., and Lellis, P. J., 1988, Bright spots related to high GOR reservoir in Green Canyon: 58th Ann. Intemat. Mtg., Soc. Expl. Geophys., Expanded Abstracts, 761-763.

Klimentos, T., 1991, Seismic and sonic properties of lavas: Second Tech. Mtg., S. Afr. Geophys. Assoc., Expanded Abstracts, 107-111.

Luh, P. C., 1992, True-amplitude signal recovery: The Leading Edge, 11, no. 2, 13-24.

Ostrander, W. J., 1982, Plane-wave reflection coefficients for gas sands at nonnormal angles of incidence: 52nd Ann. Intemat. Mtg., Soc. Expl. Geophys., Expanded Abstracts, 216-218.

- 1984, Plane-wave reflection coefficients for gas sands at nonnormal angles of incidence: Geophysics, 49, 1637-1648.

Potts, M., Schleicher, K., Wason, C., and Ellender, S., 1982, Prestack wavelet deconvolution: 52nd Ann. Intemat. Mtg., Soc. Expl. Geophys., Expanded Abstracts, 8-10.

Russell, B. H., 1988, Introduction to seismic inversion methods: Soc. Expl. Geophys., 10-l to 10-15.

- 1990, AVO inversion: Theory and practice: 60th Ann. Intemat. Mtg., Soc. Expl. Geophys., Expanded Abstracts, 1456-1458.

Rutherford, S. R., and Williams, R. H., 1989, Amplitude-versus-offset variations in gas sands: Geophysics, 54, 680-688.

Smith, G. C., and Gidlow, P. M., 1987, Weighted stacking for rock property estimation and detection of gas: Geophys. Prosp., 35, 993-1014.

Walden, A. T., 1991, Making AVO sections more robust: Geophys. Prosp., 39, 915-942.

Wiggins, R., Kenny, G. S., and McClure, C. D., 1984, A method for determining and displaying the shear-velocity reflectivities of a geologic formation: European patent application no. 83300227.2, Bull 84130, July 25.